Characterization of plastic formability and failure mechanisms in FDM additively manufactured PETG and PCL sheets

A. Rosa-Sainz [a], I. Ferrer [b], M.L. Garcia-Romeu [b,*], G. Centeno [a]

[a] Department of Mechanical and Manufacturing Engineering, School of Engineering, University of Seville, 41092, Seville, Spain
[b] University of Girona, Department of Mechanical Engineering and Industrial Construction, Girona, Spain

ARTICLE INFO

ABSTRACT

This research work presents an experimental investigation on the formability and failure of additively manufactured polymer sheets. To this regard, Nakajima formability tests following different principal strain paths have been conducted on 2 selected FDM-printed polymer sheet materials, polyethylene terephthalate glycol and polycraprolactone, this being carried out for the first time ever, as far as the plastic behavior and formability study of this kind of 3D printed materials has been limited so far uniquely to conventional tension or compression tests. The analysis includes the evaluation of the different types of failure under plastic deformation for each material considered, allowing the assessment of the overall formability limits within the materials forming limit diagrams combined with the failure evaluation performed via optical microscopy. Thus, the results provided the overall characterization in terms of sheet formability and the comprehensive assessment of the different failure modes and the forming conditions upon which each type of failure is attained for each of the two printed materials. Furthermore, these results allow the authors to create an essential evaluation framework for the ongoing research on process hybridization including the combination of 3D printing technologies with innovative forming processes such as incremental sheet forming.

1. Introduction

Manufacturers constantly search for new technologies to satisfy all aspects of the growing demand of the market. For this purpose, additive manufacturing (AM), which started out as a rapid prototyping technique, is nowadays revolutionizing and decentralizing industrial production. There are several AM technologies available for metal, polymer and, more recently, for composite materials [1], sharing several benefits, being one of the most notable is the reduction in time required to bring a product to market, achieved through the acceleration of the prototyping process and a decrease in the costs associated with product development [2]. Furthermore, the range of AM applications covers conventional to advance industries as aerospace or the automotive [3], attracted by the light weighting of structures in the search for green mobility, superior fuel efficiency, and handling. Beyond that, the biomedical sector is also in the list of applications of AM due to its interest in the manufacturing of customized prostheses [4,5] or in tissue engineering appealing to the possibility of the manufacturing of personalized scaffolds that allow the integration of medicalization [6–8].

Among all the available AM technologies, Fused Deposition Modeling (FDM) (see Fig. 1a), also known as 3D printing, Fused Filament Fabrication (FFF) or in a new and broad consideration as Material Extrusion (MEx), is being a widely used option and a profitable opportunity. Furthermore, due to the ease of printing and the use of advanced thermoplastics such as Polyether ether ketone (PEEK) [9], polymers are receiving increasing interest for the production of lightweight and structural parts.

The main research activities in the field of AM, and particularly in FDM, are focused today on investigating a number of the printed components such as thermal conductivity, electrical conductivity or chemical resistance [10–14]. However, a significant number of research works in the field of AM/FDM aim to evaluating their mechanical properties, including tensile strength, flexural strength or impact resistance both for virgin or combined materials. Related to this, some reviews have recently come to light that include recommended guidelines in a standardized approach that can allow the comparison of published results and help in the development of FDM technology for advanced applications [15]. Other work documents the latest advances in interface printed parts to provide a complete understanding of the process, structure, and interlayer bond for this technology [16].

As has just been pointed out, the mechanical characterization of printed parts is capturing enough research attention as FDM continues to advance, since there is still the problem of converting printed parts into functional components for actual use. To this regard, researchers have been mainly focused on understanding and evaluating the mechanical properties due to the weak and anisotropic mechanical behavior of the 3D printed components compared to those obtained by conventional processing. In the specific case of FDM, the lack of appropriate standards, specifically designed to consistently test the tensile properties of polymeric parts and compare them with common products, is a major obstacle to the wide application of additively manufactured polymer parts in industry [17].

Related to that, very few papers have dealt so far with the evaluation of the plastic behavior of 3D printed materials, neither in FDM nor in any other AM technology. As exposed above, the work analysing 3D printed parts formability is limited to the material plastic characterization via uniaxial tension (or compression) tests. However, there is a lack of knowledge about other plastic behavior properties including their evaluation under different strain paths. This factor is of key importance in process hybridization, including the combination of AM technologies with conventional sheet-forming processes or even innovative processes such as incremental sheet forming. One of the main limitations of using incremental sheet forming for a certain purpose, such as the manufacture of biocompatible sheet prostheses, is that the definition of the sheet blank is limited by the industrial suppliers. In this respect, not every thickness might be potentially available and sometimes the blank geometries need previous machining operations that may not be suitable in the biomedical sector. Thus, the use of AM technologies could allow manufactures to obtain and design their own sheet blank including controlled materials, shapes, and thicknesses, in this latter case allowing blank with variable sheet thickness that could be suitable, after forming and the expected local thickness variations, for certain analytical contours. Beyond that, sheet forming allows for, in many cases, the improvement of certain materials properties such as the material strength via yielding.

In this context, sheet formability is the term used to determine the degree of deformation to which a sheet material can be subjected during a forming process following a specific strain path. This deformation can be evaluated using the in-plane principal major strain (ε_1) and minor strain (ε_2) in the so-called forming limit diagram (FLD) (schematically depicted in Fig. 1b). Indeed, FLD is an experimental analysis tool in which the major strain is represented on the ordinate axis and the minor strain on the abscises axis in the Cartesian plane, and it presents the deformation state of the material, the relation between the minor strain ε_2 and the major strain ε_1 the strain ratio (β), and is given by $\beta = \varepsilon_2/\varepsilon_1$. The understanding of the limits of formability within the principal strain space enables the development of a comprehensive framework for analyzing fracture limits, which is crucial in sheet forming processes. Although there are widely used and validated techniques to determine necking and fracture in sheet metal forming, there is an absence of dedicated methodologies and procedures for polymers, since the formability of these types of materials is influenced by several factors, including the molecular structure, molecular weight, orientation of the polymer chain, temperature, strain rate, and presence of any fillers or additives [18]. In this context, Rosa-Sainz et al. [19] adapted methodologies commonly used in sheet metal forming for polymeric sheets, with the goal of determining the formability limits by necking and fracture. These methodologies were validated for various polymeric sheets, including polycarbonate (PC) [19,20], polyether ether ketone (PEEK) [9], and ultra-high molecular weight polyethylene (UHMWPE) [21].

In this global context, the objective of this experimental investigation is to apply for the first time ever the previously described methodologies to this new kind of polymeric sheet materials, i.e. FDM additively manufactured polyethylene terephthalate glycol (PETG) and polycraprolactone (PCL) sheets, in order to characterize the formability limits by necking and fracture and obtain the resulting materials forming limit diagram or FLD. The experimental work is conducted by performing Nakajima tests at room temperature using four different geometries corresponding to the same number of strain paths from tensile strain towards equibiaxial strain for both PETG and PCL sheets.

The results are provided not only in terms of the limiting strain assessed within the FLD material but also analyzing the different modes of failure attained and the testing conditions upon which each type of failure is attained. In this sense, different kinds of failure occurred depending on those testing conditions and strain paths considered, including localized necking, ductile fracture, and a rare failure phenomenon identified by the authors as interlayer gliding.

In summary, a significant contribution of this research work lies in being the first time, as far as the authors are aware, that Nakajima tests are used to characterize additively manufactured sheets. Additionally, this allowed the assessment of the different modes of failure, including the new limit within the FLD of the PCL sheet defined by failure via interlayer gliding. Finally, it must be pointed out that this experimental
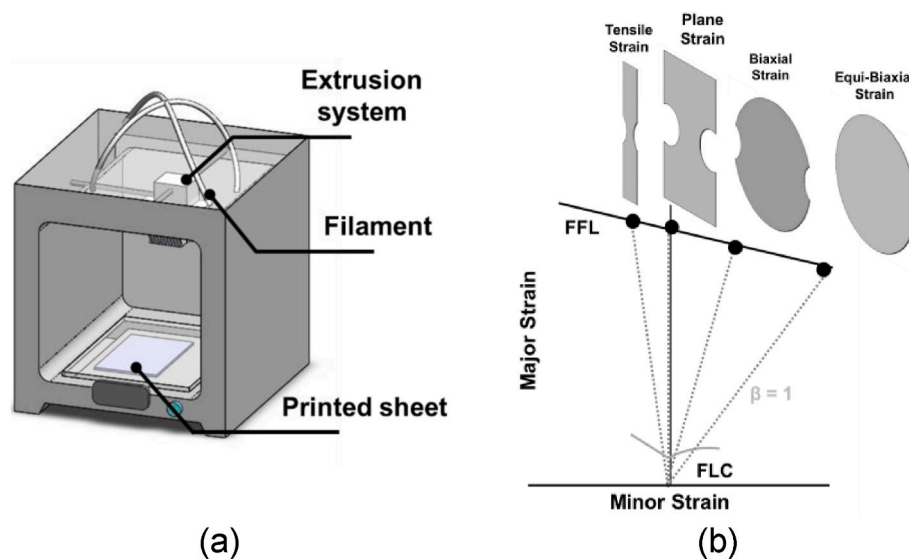

Fig. 1. Schematic representation of (a) fused deposition modeling and (b) forming limit diagram (FLD) depicting the FLC or Forming Limit Curve and the FFL or Fracture Forming Limit.

analysis allows the authors to create an essential evaluation framework for subsequent evaluation in incoming research papers dealing with process hybridization, including the combination of additive manufacturing with innovative forming processes such as ISF or other, enabling the utilization of this hybridization for various applications.

2. Methodology

This section includes the methodology employed, which is divided into the 3D printing of PETG and PCL sheets, and the subsequent characterization of these printed sheets utilizing Nakajima tests within the framework of additive manufacturing.

2.1. 3D printing

The investigation was carried out on sheets of polyethylene terephthalate glycol (PETG) and polycaprolactone (PCL) both with 2 mm thickness, obtained by fused deposition modeling (FDM). PETG material with a diameter of 2.85 mm was provided by Smart Materials 3D, while Facilian™ PCL 100 filament, with a diameter of 2.85 mm, was acquired from the 3D4MAKERS™ material supplier.

Table 1 indicates the mechanical properties of the 3D4MAKERS™ PETG filament material and the Facilian™ PCL 100 filament. According to the material supplier, the mechanical properties of PETG were tested using tensile tests according to the ASTM D638 standard and impact tests according to the ASTM D256 standard. For PCL material, tensile tests were performed according to the ISO 527-1 standard and impact tests following the ISO 180-1 standard.

The Ultimaker S3 3D printer was used to print the material sheets, and Table 2 contains the printing parameters used, whose values were determined on the previous works [22] and some previous tests carried out in the laboratory.

Regarding the PCL, the printing temperature was established at the highest values of the supplier"s recommended range to avoid clogging of the print cores, maximize the material flowability, and minimize the internal porous. With respect to the recommended PETG temperature, a data sheet was used. As will be seen and expected, temperature will be an important parameter that affects layer composition of the sheet and its formability. The other important process parameter is the height of the layer, which also significantly affects the printing quality of sheets, so with greater layer heights exhibited earlier cracking and breakage and cracking [22]. As a general guideline, layer heights between 0.08 and 0.3 mm were considered suitable for 0.4 mm nozzles, although the best results were obtained with sheets printed at 0.08 and 0.1 mm without much variation between them. Thus, the 0.1 mm setting was selected due to a substantial reduction in the printing time. 100 % infill density was established for all manufactured specimens to imitate the conditions of a homogeneous and isotropic solid structure [23,24]. The printing pattern also played a crucial role in forming behavior, just as it affects the results of mechanical properties [22].

2.2. Material characterization

This section contains the methodology followed to determine the formability limits by necking and fracture for sheets manufactured by

Table 1
Mechanical and thermal properties of PETG and PCL materials at 25 °C extracted from suppliers.

	PETG	PCL
Density (g/cm^3)	1.27	1.1
Tensile strength (MPa)	50	45
Tensile modulus (MPa)	2100	350
IZOD Impact Strength (kJ/m^2)	8.1	8
Melting temperature (°C)	260	60

Table 2
Printing parameters for PETG and PCL polymeric materials.

Printer parameters	PETG	PCL
Layer height (mm)	0.1	0.1
Wall line count	3	3
Infill density (%)	100	100
Printing temperature (°C)	250	160
Build plate temperature (°C)	60	60
Print speed (mm/s)	75	50
Printing direction	−45/+45	−45/+45

3D printing with PETG and PCL. The methodologies were adapted from those commonly applied from metals to polymeric sheets and were used for the first time in Ref. [19]. The Nakajima geometries were printed using FDM, and subsequently, peripherical finishing machining was carried out on their notch zones to improve the surface quality and prevent stress concentrations, ensuring a defect-free surface and preventing premature failure. These specimens were identified as tensile strain (TS), plane strain (PS), biaxial strain (BS), and equibiaxial strain (EBS). The dimensions of the specimens and operating conditions for the geometries considered are presented in Table 3. The punch speed was set at 1 mm/s, following the recommended conditions described in standard ISO 12004–2:2008 [25]. Regarding the clamping force, the necessary force was applied to properly secure the sheet. For PCL, 30 kN was used, while for PETG, 10 kN was used. This difference was due to PETG experiencing tearing if a force greater than 10 kN was applied as the punch ascended.

One limitation of 3D printing is that each sheet may have a slightly different thickness from one print to another. To minimize these differences, batches of sheets were printed and only those with a thickness of 2 ± 0.05 mm were selected to ensure that all test pieces had the correct thickness. To ensure the repeatability of the results, three replications of each geometry test were performed.

The formability limits by necking and fracture of both polymeric materials were determined using Nakajima tests following the ISO 12004-2 standard [25] on a universal testing machine (model 142–20 Erichsen) at room temperature (25 °C). The experimental setup employed to perform the Nakajima tests comprises three primary components: (i) a universal sheet testing machine, (ii) a digital image correlation (DIC) system, and (iii) a force and displacement acquisition system. A schematic representation of this setup is provided in Fig. 2a. In the Nakajima test, the specimen is placed between the blank holder and the backing plate, and the punch is scrolled until the specimen fractures, or the race end is reached. Strain measurements in the deformation area were obtained using the DIC system (ARAMIS® v6.2.0 6, GOM, Germany), which is equipped with 2 CCD cameras with an angle of 23.6° between them and a lens with a focal length of 50 mm (see the schematic representation in Fig. 2a). Image acquisition was set at 12 frames per second with a facet size of 13 × 11 pixels. The DIC system requires a black and white stochastic pattern on the surface of the specimen, which was obtained by spraying matte black on a white background, resulting in the stochastic pattern. To minimize friction between the punch and the polymeric specimens, we sandwiched a layer of polytetrafluoroethylene (PTFE) between two layers of Vaseline.

The formability limits by necking and fracture of both polymeric materials were characterized by Nakajima tests. In this sense, necking is a mode of failure that occurs under tension when large amounts of strain are disproportionately located in a small region of the material. The time-dependent methodology previously described by Ref. [7] was used to detect the onset of necking in 3D printed polymeric sheets in this experimental research. This approach is based on experimental evidence of initiation and development, and uses the temporal analysis of major strain ε_1 and its first-time derivative $\dot{\varepsilon}_1$, or major strain rate, for a series of points along a section perpendicular to the necking area. Previous research by the authors [7] showed that the original approach needed to be adapted to account for the contrast between the localized thinning

Table 3
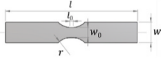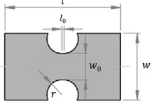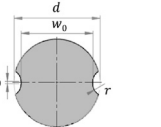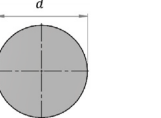Summary of the experimental work plan for PCL and PETG specimens.

Test geometry	Specimen		Operating conditions		
	Geometry	Dimensions (mm)	Blank holder force (kN)		Velocity (mm/min)
			PCL	PETG	
Tensile strain (TS)		$l = 200$ $w = 30$ $l_0 = 5$ $w_0 = 15$ $r = 25$	30	10	60
Plane strain (PS)		$l = 200$ $w = 114$ $l_0 = 4$ $w_0 = 45$ $r = 25$	30	10	
Biaxial strain (BS)		$l_0 = 5$ $w_0 = 150$ $r = 25$ $d = 182$	30	10	
Equibiaxial strain (EBS)		$d = 182$	30	10	

Table 4
Shows the pair of neck strains obtained for the TS specimen by applying the time-dependent approach. The results indicated that the strain levels were nearly identical for the three specimens considered. The principal strain at necking and fracture evaluated using the DIC system are presented in Table 4 along with the standard deviation of these results. As explained in Section 2.2, these fracture strains allow the determination of the FFL.Table 4. Summary of the necking and fracture results for PETG material.

Test geometry	Repetition	Onset of necking	
		$\varepsilon_{1,lim}$	$\varepsilon_{2,lim}$
TS_PETG	I	0.083	−0.017
	II	0.084	−0.015
	III	0.087	−0.013
	Mean	0.084	−0.015
	Standard deviation	0.0021	0.002
		Onset of fracture using DIC	
TS_PETG	I/II/III	0.2079/0.1993/ 0.2199	−0.0656/-0.0565/- 0.0634
	Mean	0.2088	−0.0618
	Standard deviation	0.0103	0.0047
PS_PETG	I/II/III	0.1824/0.1756/ 0.1791	−0.0021/-0.0056/ −0.0043
	Mean	0.1790	−0.004
	Standard deviation	0.0034	0.0017
BS_PETG	I/II/III	0.1496/0.1562/ 0.1587	0.0367/0.0402/0.0391
	Mean	0.1547	0.0386
	Standard deviation	0.0047	0.0018
EBS_PETG	I/II/III	0.1568/0.1672/ 0.1593	0.0432/0.0501/0.0456
	Mean	0.1610	0.0462
	Standard deviation	0.0054	0.0035

characteristic of metals and the necking behavior of polymers.

In this context, Fig. 2b schematically shows the Nakajima test of the TS specimen, indicating a series of points on the surface of the specimen to establish the instability region of the necking zone. The process for applying the time-dependent methodology is detailed as follows: (i) Identify the two reference points at the necking zone: point A and point B (PA and PB). Point A corresponds to where necking starts, and point B is the first point where strain starts to decrease. The representation of the major strain with time was carried out for several points along a section perpendicular to the necking site (e.g., points PA, P1, …, PN, PB) was carried out to identify these two points (see Fig. 2b). (ii) Identify the boundary of the instability region between point A and point B. This region allows one to observe how the points have a monotonic increase in strains, which ceases at point B (see Fig. 2b). (iii) Fig. 2c represents the evolution of the strain rate of point B with time. The methodology assumes that the onset of necking occurs at the instant when the strain rate for point B reaches a local maximum (point B strain rate max in Fig. 2c). (iv) Finally, the limit strains at the onset of the necking will correspond to the strains at point A (depicted in Fig. 2c) at the instant of time "t necking".

Regarding fracture formability limits, the authors in previous experimental work [9,19,20] discussed that the initial methodology for determining the fracture forming limit in metal sheets [26] must be adjusted for polymers due to the propagation of necking in polymers along the entire length of the specimen. In this regard, due to the relatively low value of the Young modulus of elasticity of polymeric materials compared to metallic materials, significant material elastic recovery occurs after fracture. For this, the methodology included in Ref. [19], shown that it was more accurate to consider that the minor fracture strain at fracture (designated as ε_{2f}^*) is obtained considering that the slope of the local strain loading path slope (i.e. $\beta^* = \varepsilon_2/\varepsilon_1$) remains constant. The slope (β^*) was obtained at the last measured strains by DIC system $(\varepsilon_1^{DIC}, \varepsilon_2^{DIC})$ as: $\beta^* = d\varepsilon_2^{DIC}/d\varepsilon_1^{DIC}$ for determining the fracture forming limit (FFL). More details on this methodology can be found in Ref. [19]. In addition to the time-dependent method, the evolutions of forces and displacement will be analyzed for each material and each specimen, with the aim of qualitatively assessing the presence of plastic instability leading to necking [27].

3. Experimental results

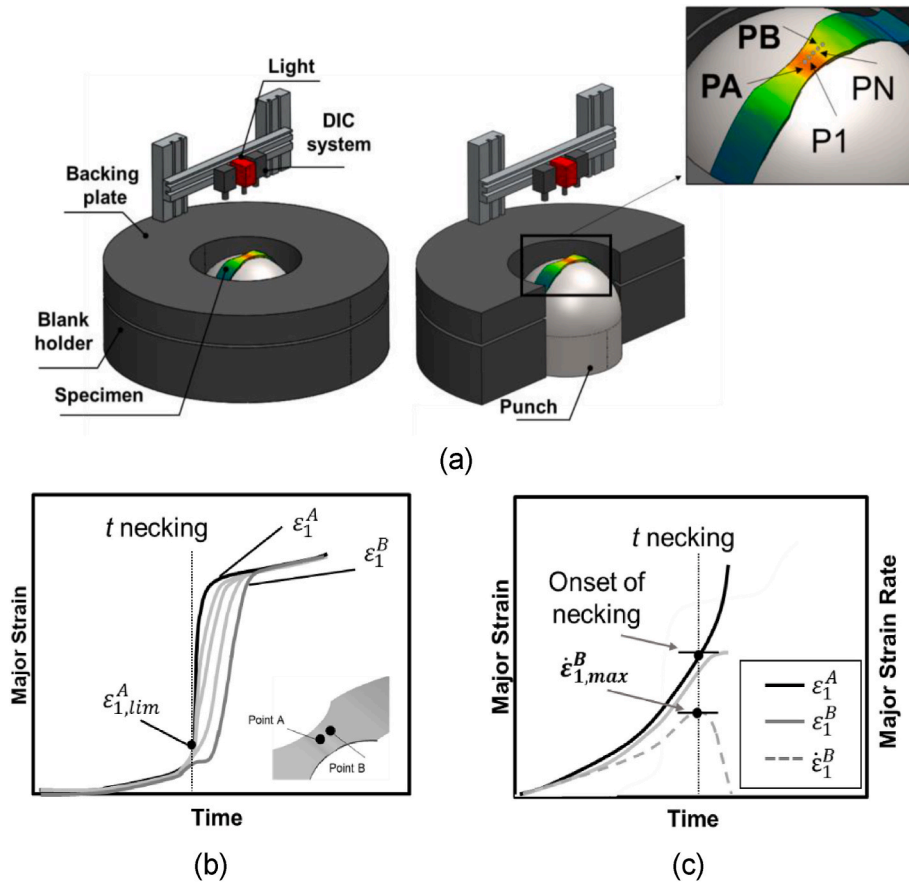This section presents the results of applying the previous

Fig. 2. (a) Schematic representation of the Nakajima test. (b) Evolution of the major strains over time for the necking region and (c) the time-dependent approach adapted from Ref. [19].

methodologies described in section 2 to the evaluation of the formability limits by necking and fracture for PETG and PCL with 2 mm thickness materials.

3.1. PETG

This section shows the results obtained for PETG material, including the results for determining the formability limits by necking and fracture to establish the PETG forming limit diagram in principal strain space. As stated in Section 2, PETG Nakajima specimens were 3D printed with different geometries, including TS, PS, BS, and EBS.

3.1.1. Necking and fracture analysis

Fig. 3 presents the time-dependent approach to the PETG TS Naka-jima specimen. Fig. 3a shows the evolution of points located on a perpendicular section to the necking area to establish the instability zone (i.e., between Point A and Point B). Additionally, the major strain distribution obtained by the ARAMIS® system is indicated in Fig. 3a. Fig. 3b shows the evolution of the major strain with time for Point A and Point B, as well as the major strain rate for Point B. In this sense, the evolution of the major strain rate for Point B enabled identification of its local maximum and thus the instantaneous time of the onset of necking. The methodology used allowed for the determination of the limit strains
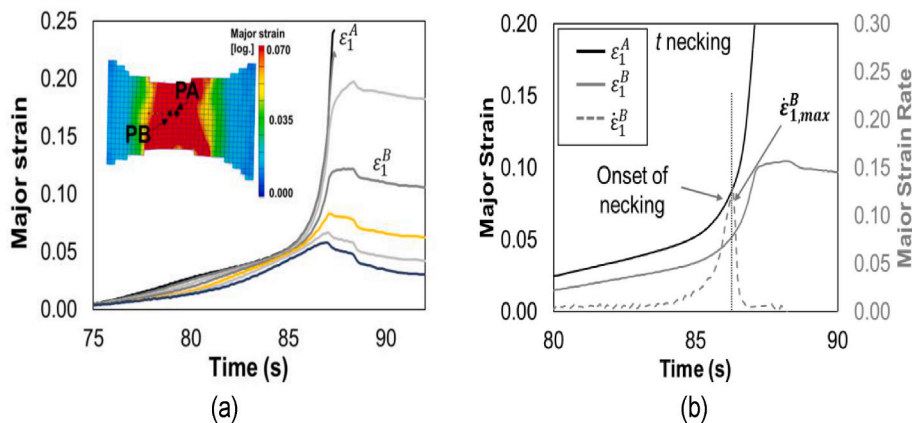

Fig. 3. Application of the methodology to obtain the onset of neck strains for a TS Nakajima specimen. (a) Experimental time evolution of the major strain along the points of the selected section. (b) Application of the time-dependent approach.

at the point of the onset of necking, which corresponded to the strains at Point A during the TS PETG Nakajima specimen at a specific moment in time.

Fig. 4a, b, and 4c show the attempt to apply the time-dependent approach for PS, BS, and EBS Nakajima specimens, respectively. The approach revealed that the strain of a series of points along a section perpendicular to the necking area did not show cessation, as previously observed for the TS PETG Nakajima specimens. The analysis of the major strain evolution for PS, BS and EBS over time revealed that the point A, where necking begins, undergoes the most significant deformation and eventually leads to the fracture of the specimen. On the other hand, the other points undergo a gradual deformation and do not achieve higher strains, as the specimen fractures before they can continue to deform further. The conclusion drawn was that the neck was not discernible through the time-dependent approach, as evidenced by examining the points in a perpendicular section, and no deceleration was observed. As a result, it was not feasible to identify point B, and thus, the instability region could not be determined using the time-dependent approach for PS, BS and EBS specimens.

The analysis utilizing a time-dependent methodology revealed the PETG Nakajima onset of necking in the TS specimen, in addition, it was indicated that necking was not a mode of failure for the PS, BS, and EBS Nakajima specimens. This conclusion was supported by the analysis of the force-displacement behavior, as depicted in Fig. 5a, which displays a slight reduction in force at the moment of necking for the Nakajima TS test, and by the uniform distribution of the major strain for Nakajima PS,

BS and EBS tests up to failure by fracture. As can be observed for the four specimens, the force-displacement curve shows noise throughout the test. This phenomenon may be due to the low adhesion between the layers of printed material, in the case of PCL, as will be seen later, this observation in the force-displacement is not quite as noticeable. Furthermore, Fig. 5b depicts the Nakajima specimens after testing, as can be observed, the material exhibits a lack of ductility, breaking at a low degree of deformation.

Fig. 6 shows the fractographies of the examined specimens, which were analyzed using a NIKON® SMZ800 N at a magnification of ×10. The specimens were sectioned along the indicated dotted red line in each image, polished, and subsequently observed on the surface using an optical microscope. In general, for polymers, three distinct regions are clearly discernible: the necking zone (indicated as "I"), the transition zone (marked as "II") and the fracture zone (represented as "III") [28]. The neck zone represents the area where significant localized deformation occurred, while the transition zone denotes the boundary between the neck region and the elongated area. The fracture zone denotes the location where the specimen experienced a fracture.

In Fig. 6a, the cross sectional fractography of the TS specimen can be observed, along with the TS specimen to the right of the image. In this fractography, a local necking (marked I) can be observed in the specimen, with a smooth transition zone (II) between this necking and the undeformed area, followed by an open fracture (marked III). Additionally, a second necking is observed in this specimen, indicated by a white rectangle, where a transition zone in the local necking can be observed.
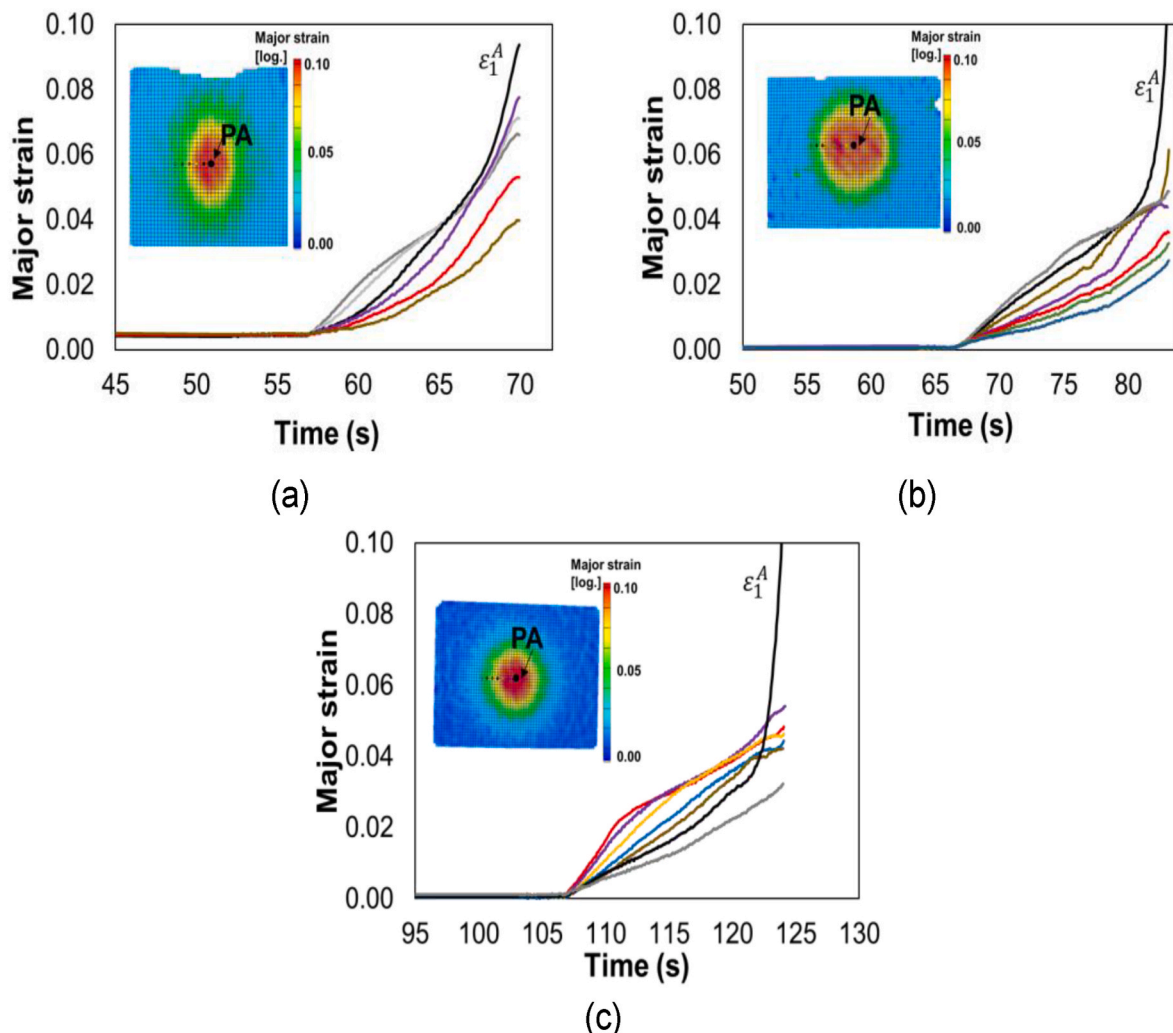

(a)

(b)

(c)

Fig. 4. Experimental time evolution of the major strain along the points of the selected section for (a) PS, (b) BS and (c) EBS PETG Nakajima specimens.
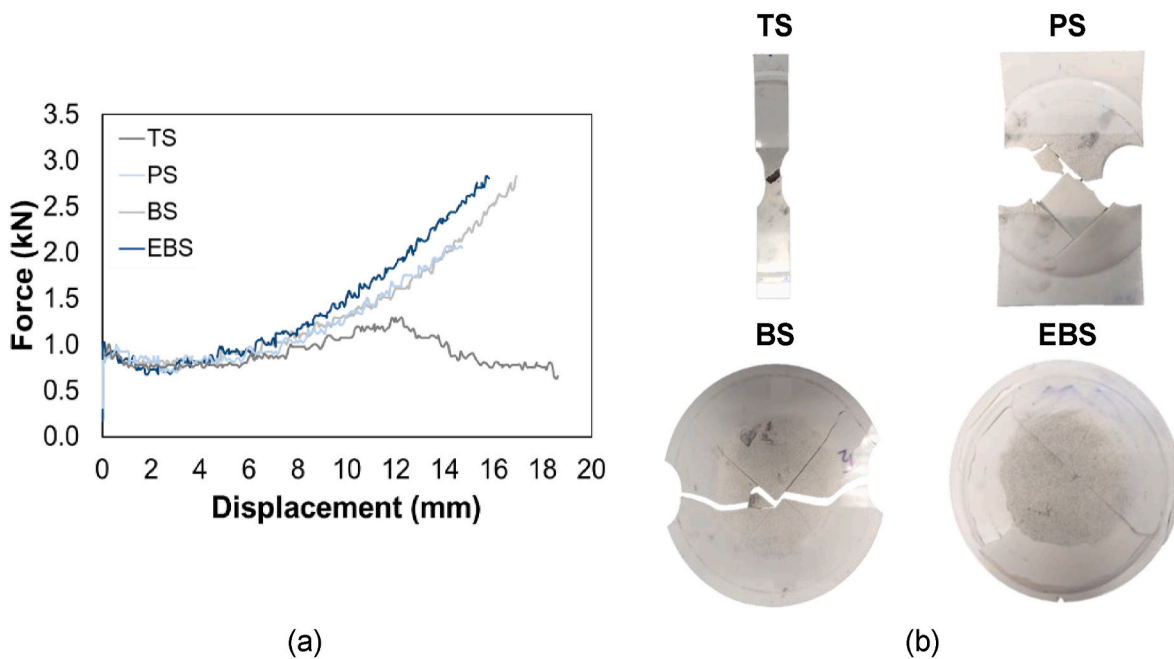
Fig. 5. (a) Force displacement for PETG Nakajima tests and (b) specimens after fracture.
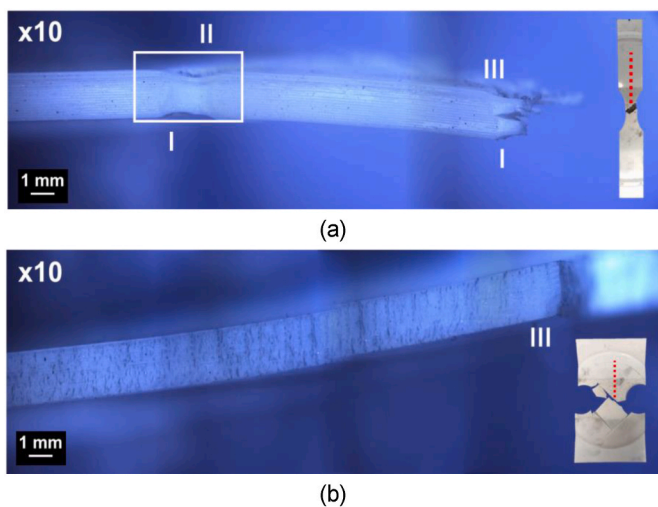

Fig. 6. Fractography of PETG Nakajima specimens: (a) TS and (b) PS.

In Fig. 6b, the fractographic analysis of the cut section of the PS specimen is depicted, accompanied by the PS specimen positioned to the right within the image. In contrast to the previous TS Nakajima specimen, the presence of a visually distinguishable neck zone was not observed in this particular specimen, as determined by time-dependent analysis. The fractography only revealed the presence of the fracture zone. Furthermore, fractographies of both BS and EBS specimens were performed in order to validate the absence of localized neck failure mode.

3.1.2. Failure modes

Fig. 7 presents the fractographies of the TS and EBS specimens for the purpose of analyzing their mode of failure. According to the literature [29], the fracture process of printed parts is primarily attributed to the additive manufacturing process that leads to delamination between adjacent layers of welded material. Porous regions or inadequate interlayer bonding (light delamination) can serve as a point of crack initiation and result in premature failure of components. The results of

the Nakajima tests indicate that PETG exhibits a ductiless fracture. The fractography of the TS specimen in Fig. 7a depicts another instance of the TS specimens conducted to ensure repeatability. In this context, it presents a fracture termination slightly different from that of the TS specimen depicted in Fig. 6a, specifically with a more tightly closed fracture observed in this case. In both fractographs (TS and EBS specimens), the printed layers in the material can be observed.

As described in section 2.2, the Nakajima tests were conducted at 60 mm/min as indicated in the ISO standard for the determination of the FLC in sheet metal [25]. The results of the PETG material subjected to these tests showed a lack of ductility in the material when tested at the mentioned speed. In this sense, this result is consistent with the findings of the study conducted by Ergene and Bolat [30], where uniaxial tensile tests were performed on PETG AM manufactured specimens at three different test speeds: 5 mm/min, 25 mm/min, and 50 mm/min. Failure was evaluated through inspections of deformation on both macro and micro-scales. The results showed that PETG specimens underwent ductile deformation at a low test speed of 5 mm/min, and as the test speed increased, mixed-mode mechanisms became increasingly dominant, leading to completely brittle damage observed in the PETG specimens at test speeds of 25 mm/min and 50 mm/min. Mercado-Colmenero et al. [31] found the same result for AM-made PETG material, revealed that the fracture process of structural elements manufactured in the Z direction was the result of the delamination and breakage of the plastic filaments in the adjacent layers located on the supports. Furthermore, the study [31] demonstrated that this form of fracture is not completely brittle, as the plastic material undergoes a hardening process through plasticization in the regions where the fractures are propagating.

3.1.3. FLD

Fig. 8 shows the PETG 3D printed sheets in the forming limit diagram (FLD) in principal strain space. In the FLD, the principal strain path of one representative test for each Nakajima geometry is presented. However, it must be pointed out that at least 3 successful tests were conducted for each geometry in order to provide statistical meaning to the results. For both necking (to determine the forming limit curve, FLC) and fracture strains (to determine the fracture forming limit line, FFL), the mean value of the corresponding principal strain results is depicted
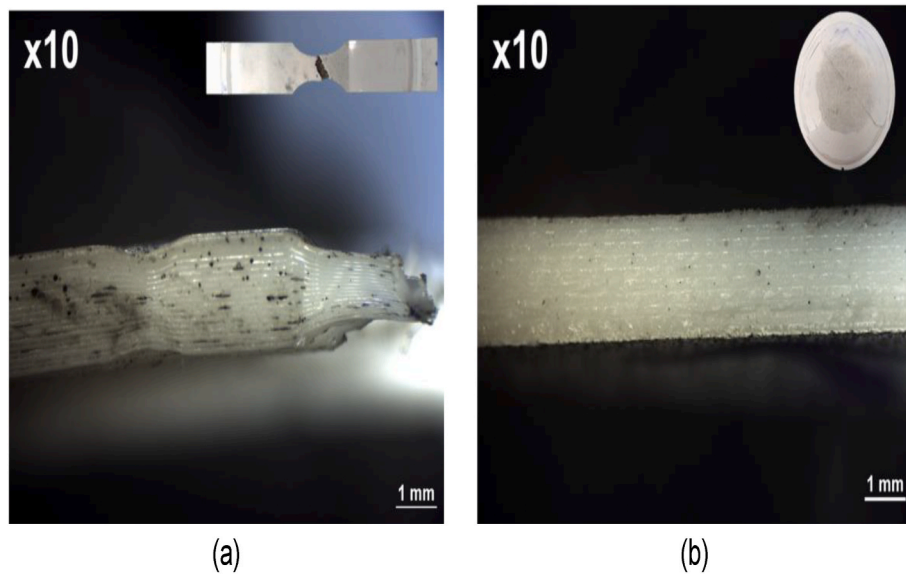
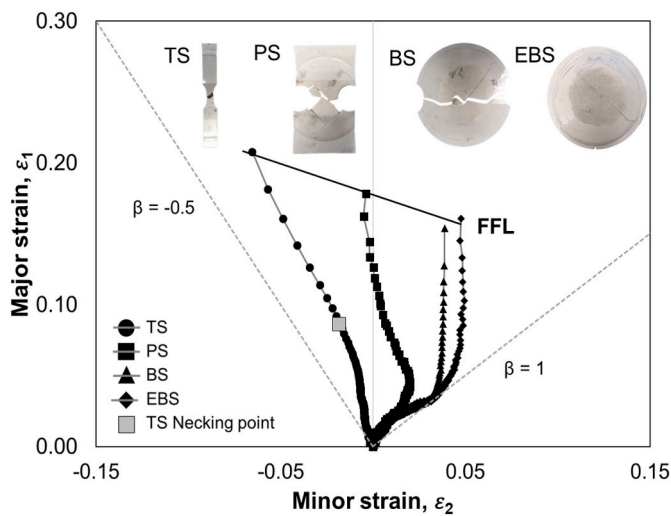**Fig. 7.** Layer observation in (a) TS and (b) EBS Nakajima PETG specimens.

Fig. 8. Formability limits for 3D printed PETG sheets with 2 mm thickness obtained by means of Nakajima specimens.

in the FLD. Only the TS specimen demonstrated necking as a failure mode. Consequently, the FLC curve was not included. Instead, a gray square represents the strain pairs at the onset of the neck, corresponding to the conditions of the TS specimen. The FFL was constructed using black solid markers, which correspond to the strain pairs at the final DIC measurement according to the methodology explained in section 2.

Upon examination of the strain paths, it was observed that the TS specimen approached $\beta = -0.3$, which was a result of its initial geometry. The PS specimen adhered to the plane strain path imposed by its initial geometry. Regarding the BS and EBS specimens, at the beginning of the test the strain paths follow a condition of biaxiality and equibiaxiality, but then they change towards a plane strain condition (at approximately a major strain of 0.04 for both specimens, as can be seen in Fig. 8). When the punch starts to contact the surface of the sheet, the side in contact with the punch might be under compression, whereas the other side is under tension. As the punch progresses, the tension on the outer surface of the sheet induces these layers to fracture. The observed change for BS and EBS may be due to the intrinsic characteristics of the printed material and the printing process. Nevertheless, a more in-depth

study would be needed to understand the reasons that may cause this clivage of the strains under these conditions.

3.2. PCL

This section outlines the findings concerning the PCL material, explained in necking and fracture analysis, discussion of failure modes, and the obtained forming limit diagram.

3.2.1. Necking and fracture analysis

PCL sheets were printed to obtain Nakajima specimens with different geometries, including tensile strain (TS), plane strain (PS), biaxial strain (BS), and equibiaxial strain (EBS).

Fig. 9 shows the application of the time-dependent approach to Nakajima specimens TS (Fig. 9a and b) and PS (Fig. 9c and d), along with a specimen image of the major strain provided by the DIC system. For the PCL TS Nakajima specimen, the time-dependent approach allowed the identification of Point A and B, which defined the instability region (Fig. 9a), where point B is the first point where the strain starts to decrease (Fig. 9b). By means of the evolution of the strain rate for Point B, the local maximum was clearly identified $\dot{\varepsilon}_{1,max}^{B}$ and thus, the time instant at the onset of necking $t_{necking}$. Finally, this approach allowed to obtain the limit strains at the onset of necking that correspond to the strains at point A strains, $\varepsilon_{1,lim}, \varepsilon_{2,lim}$ at the time instant $t_{necking}$.

Fig. 9c and d shows the application of the time-dependent approach for a PS Nakajima specimen, which was similar to the previous case (TS specimen). The instability region was defined between point A and Point B, with Point B being the first point where the strain begins to decrease (see Fig. 9c). Fig. 9d allowed the determination of the local maximum $\dot{\varepsilon}_{1,max}^{B}$ for Point B to establish the onset of necking.

Table 5 contains the pair of neck strains obtained for the TS and PS specimens by applying the time-dependent approach. The results showed that the strain levels were nearly identical for the three specimens considered and for each of the geometries. Additionally, Table 5 presents the strain measurements obtained by the DIC system, alongside their corresponding standard deviations. As explained in Section 2.2, these strain values are used to determine the FFL.

Fig. 10 shows the application of the time-dependent methodology to BS and EBS Nakajima specimens. Starting with the BS specimen (as depicted in Fig. 10a), the analysis showed that the strain of a series of points along a section perpendicular to the crack did not show any
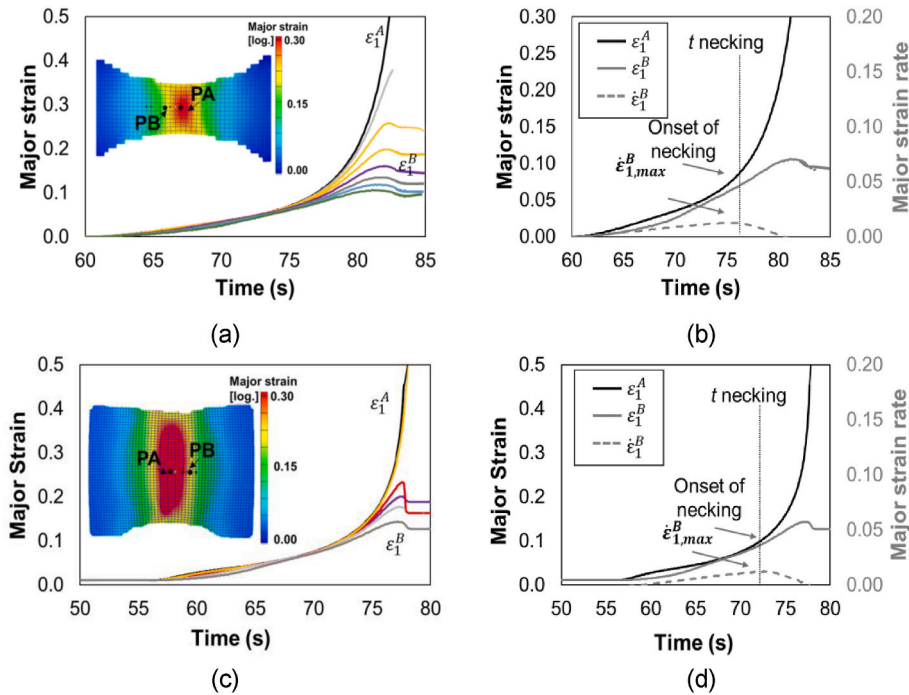
Fig. 9. Experimental time evolution of the major strain along the points of the selected section and application of the time-dependent approach: (a) (b) TS Nakajima specimen, and (c) (d) PS Nakajima specimen.

Table 5
Summary of the necking and fracture results for PCL material.

Test geometry	Repetition	Onset of necking	
		$\varepsilon_{1,lim}$	$\varepsilon_{2,lim}$
TS_PCL	I	0.119	−0.030
	II	0.116	−0.028
	III	0.112	−0.022
	Mean	0.116	−0,027
	Standard deviation	0.0035	0.0042
PS_PCL	I	0.110	0.003
	II	0.116	0.002
	III	0.113	0.003
	Mean	0.1128	0.0028
	Standard deviation	0.0027	0.0004
		Onset of fracture using DIC	
TS_PCL	I/II/III	0.8945/0.8912/0.8901	−0.0656/-0.0565/-0.0634
	Mean	0.8919	−0.1760
	Standard deviation	0.0022	0.0056
TS_PCL	I/II/III	0.9050/0.9123/0.9165	−0.04/-0.041/-0.038
	Mean	0.9112	−0.0396
	Standard deviation	0.0058	0.0015
BS_PCL	I/II/III	0.8475/0.8498/0.8325	0.3305/0.3300/0.324
	Mean	0.8432	0.3283
	Standard deviation	0.0093	0.0037
EBS_PCL	I/II/III	0.7558/0.754/0.7405	0.5825/0.5973/0.603
	Mean	0.7501	0.5942
	Standard deviation	0.0083	0.0106

decrease. The same result was observed for the EBS Nakajima specimen (see Fig. 10b), where the strain of a series of points continuously increased until the end of the test. Therefore, the derivative of the major strain of all the points studied cannot exhibit a maximum value. This observation provided the initial indication that necking may not be a mode of failure for PCL-made BS and EBS specimens. However, the DIC images showed a concentration of strain in the central region of the specimen. To establish whether necking took place in the BS and EBS specimens, an analysis of the force displacement results was conducted.

Fig. 11 illustrates the evolution of force with displacement for the geometries studied. Additionally, Fig. 11b provides a visual representation of Nakajima specimens for TS, PS, BS, and EBS. As observed, the PCL printed material demonstrated high ductility, with none of the specimens undergoing fracture during the test and reaching the maximum displacement allowed by the Erichsen testing machine. In terms of force-displacement results, a decrease in force is observed in the TS and PS specimens due to the plastic instability of the necking. In the case of the BS and EBS specimen, a smoother decrease is observed as a result of a reduction in thickness. For a thorough examination of these failure modes, a detailed analysis of the specimen fractographies was undertaken.

Fig. 12 presents the image analysis of the TS, PS, BS and EBS specimens using the optical microscope. The specimens were cut along the dotted red line indicated in each image, polished, and then observed on the surface through an optical microscope. The images were captured from the frontal plane of the specimens to detect areas of necking or its absence.

TS and PS specimens exhibited necking during the test, in this sense, different zones can be observed: designated as "I" for necking and ("II") transition zone (transition between the necked area and the elongated zone). In this case, "zone III" does not apply since none of the specimens fractured. As for the BS and EBS specimens, they displayed a new failure mode, as the specimen was capable of deforming due to the separation of its layers until it reached a state where it was practically a film. In this experimental study, the specific failure mode has been called "interlayer gliding". This failure consists in a separation of the different material layers (i.e. "interlayer") and the corresponding through thickness
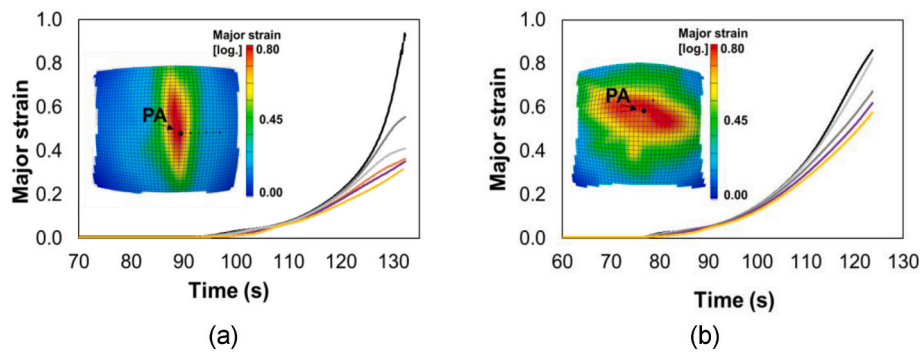
Fig. 10. Experimental time evolution of the major strain along the points of the selected section for (a) BS, and (b) EBS PCL Nakajima specimens.
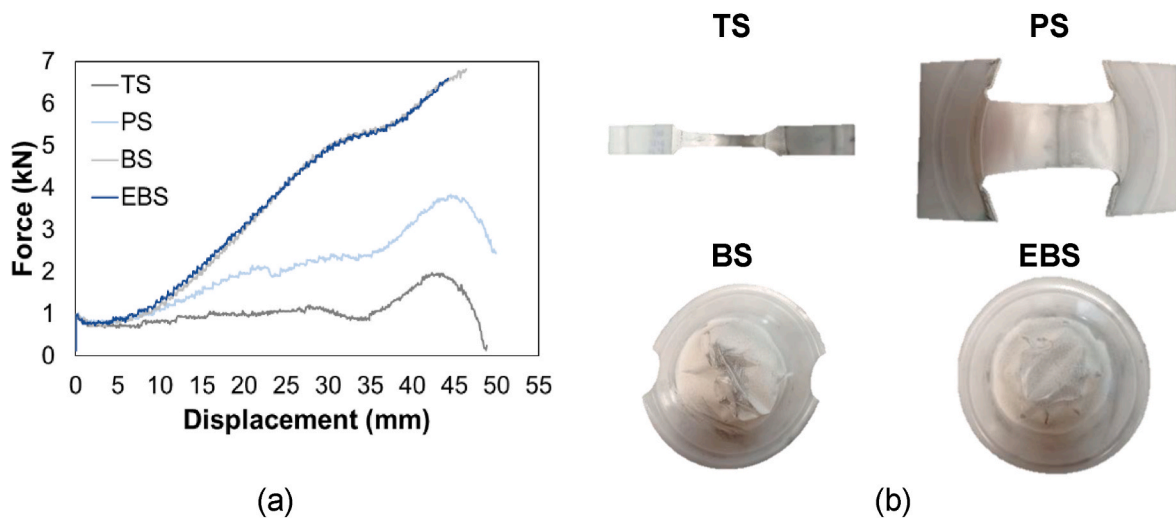

Fig. 11. (a) Force displacement for the PCL Nakajima tests and (b) specimens after fracture.

separation of those layers (i.e. "gliding"). Due to the phenomenological observation of this novel failure mode for FDM printed material plastically deformed using a punch for the first time ever (as far as the authors are aware), the term "interlayer gliding" was selected assuming that it represents this new type of failure. Here, one can observe a region where the polymer behaves akin to a film ("zone IV") and a transitional stage leading to that mode of failure ("zone V").

3.2.2. Failure modes

Fig. 13 shows the primary failure modes observed on the printed PCL sheets. From a mesoscopic view, PCL specimens exhibited strong cohesion between the printed layers, almost behaved like a conventionally manufactured polymer (see Fig. 13). As described in Section 3.2.1, localized necking could be observed in the TS specimen (Fig. 13a), whereas in the EBS specimen, a significant reduction in thickness was evident, almost reaching a thin layer or film-like behavior (interlayer gliding).

To approximate the level of strain at which the interlayer gliding failure mode occurred, the results were analyzed through the DIC system and thickness measurements were taken along the specimens. In this regard, Fig. 14a displays various points analyzed along the thickness of the EBS specimen. The logarithmic strain in the thickness direction was calculated (ε_3), and for a constant strain ratio ($\beta = \varepsilon_2/\varepsilon_1$,), the major strain was calculated (applying volume conservation, i.e. $\varepsilon_1 + \varepsilon_2 + \varepsilon_3 = 0$). Fig. 14b shows a contour graph that depicts the thickness measurements obtained along with the major strain for a set of points along the EBS specimen section. From point 7 to point 8 is when that drastic change in thickness occurred, which was also evident in the increase in

major strain. At point 7, there was a major strain of 0.39, and at point 8, a major strain of 0.7. Likewise, images extracted from the major strain of the DIC system are displayed. When analyzing the DIC images, it was noticeable how the strains were uniformly circular due to the geometry imposed by the punch (in Fig. 14c, on the left side). This strain gradually shifts to an elliptical shape (in Fig. 14c, on the right side) due to the reduction in thickness caused by layer separation. This elliptical shape continues to propagate until the film becomes clearly visible. The same analysis was conducted to determine the strains of the BS specimen. In this case, the results were similar to those of the EBS specimen, which yielded a major strain value for the gliding of 0.4.

3.2.3. FLD

Fig. 15 shows the FLD for PCL 3D printed sheets in the principal strain space. Within the FLD, one of the three strain paths examined for each Nakajima geometry is shown. The FLD displays the mean of the strain results for both necking (used to establish the FLC) and ultimate strain results (utilized for determining FFL). The time-dependent approach was successful in identifying the onset of necking in the TS and PS Nakajima specimens. The necking points for the TS and PS specimens are denoted on the FLD using gray squares. The FLC is represented as a gray straight line that extends from the TS region to the PS region. In the case of the BS and EBS specimens, the average strains obtained were represented using a black diamond symbol, characterizing a new failure curve named the "interlayer gliding line" or IGL, depicted as a dashed gray line in the FLD. This line was depicted with a 10 % scatter band shaded gray.

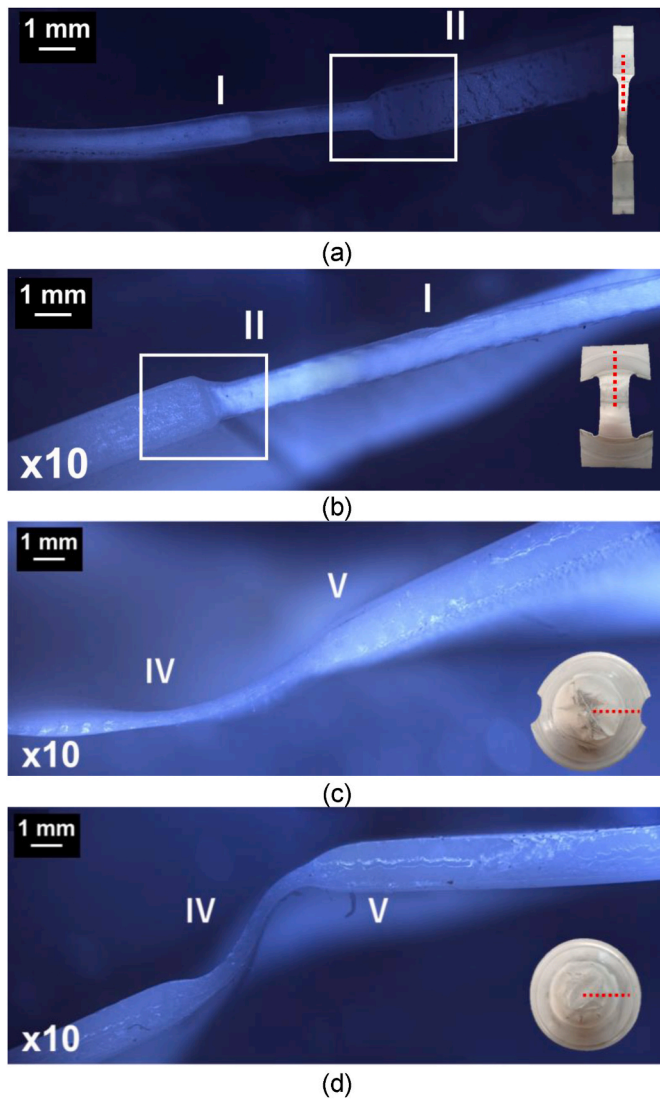The FFL was represented as a black straight line was determined

Fig. 12. Fractography of PCL Nakajima specimens: (a) TS, (b) PS, (c) BS and (d) EBS.

using the last DIC measured strain points. This procedure was also used by Rosa-Sainz et al. in Refs. [7,9,10] which showed that the FFL by DIC should be considered for polymers due to their high level of elastic recovery after Nakajima tests.

Regarding the strain paths, the TS specimen followed $\beta = -0.3$ as dictated by its geometry, with a major strain of approximately 0.4, the minor strain remained constant until the end of the test. The PS specimen showed a plane strain path in accordance with its initial geometry.

The BS specimen demonstrated a biaxial deformation path and similarly to the TS specimen, its slope underwent a change with a major strain of approximately 0.5, resulting in a constant minor strain. Finally, the EBS specimen closely followed the equibiaxial strain path imposed by its geometry.

4. Discussion evaluation

Table 6 shows the overall results of the study in terms of formability (maximum major strain obtained), maximum thickness reduction, and the type of failure found for the four geometries tested in the two polymeric materials (specimen view and enlarged view). Under the type of failure, "LN" indicates "Local Neck", "F" stands for "fracture", and "IG" represents "Interlayer Gliding".

PETG showed low formability values because of the nature of the material when manufactured by additive manufacturing (this discussion will be addressed later), resulting in a very non-ductile material whose layers separate and break as localized force is applied. The maximum thickness reduction achieved was for the BS and EBS specimens, around 18 %. Regarding the failure mode, only the TS specimen showed localized necking and eventually fracture, while the PS, BS and EBS specimens experienced a fracture of the layers themselves without localized necking initiation.

However, PCL exhibited a different behavior when manufactured through additive manufacturing. High levels of formability were achieved for all specimens tested, the maximum being for the PS specimen with a major strain of 0.91. The maximum thickness reduction was observed in the EBS specimen. Regarding failure modes, the TS and PS specimens showed localized necking that propagated until the end of the test. The predominant mode observed in BS and EBS specimens was interlayer gliding, steadily progressing throughout the test without leading to fracture, ultimately culminating in a state akin to a film at the conclusion of the test.

In Fig. 16 there is also a visual chart that summarizes all the information obtained from the results. In this sense, 3D bars are represented with blue color for the PETG material and red for the PCL material. In this context, the gauge length values are represented on the x axis to indicate the geometries of the tested specimens, which were 15 for TS, 45 for PS, 150 for BS, and 182 for EBS. On the y-axis, the failure mode is represented, which is indicated by colors: gray for local neck, yellow for the fracture, and green for interlayer gliding, and on the z-axis, the values of the maximum major strain obtained are depicted (above each type of specimen type for clearer visualization).

The strains achieved for PETG demonstrated low ductility, resulting in its own fracture. The failure mode of the local neck was exclusively manifested in the TS specimen (blue bar with 0.21 major strain in the local neck area), while in the remaining cases, it led to fracture (see blue bars in the fracture zone, PS, BS and EBS). This early fracture could pose an issue for PETG sheets and subsequent applications with this material. PCL exhibited high levels of formability, local necking was observed in the TS and PS specimens (red bars in the local neck zone), and the
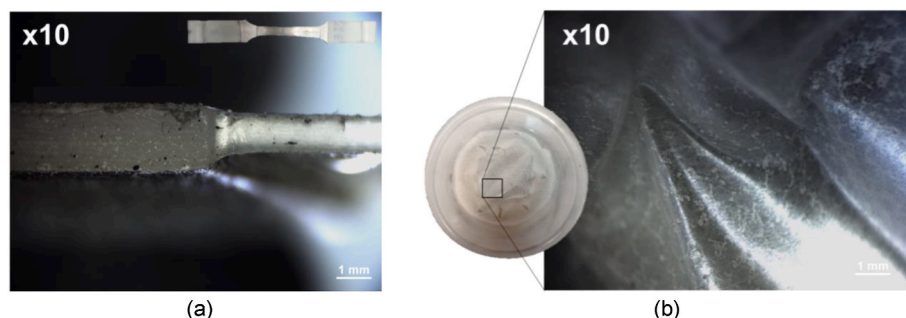

Fig. 13. Layer observation in (a) Nakajima PCL (local neck) and (b) EBS (interlayer gliding) specimens.

Failure mode view

Thickness vs. major strain across points along thickness

(a)

(b)

In-time evolution of the surface and major strain for the EBS specimen

Before interlayer gliding

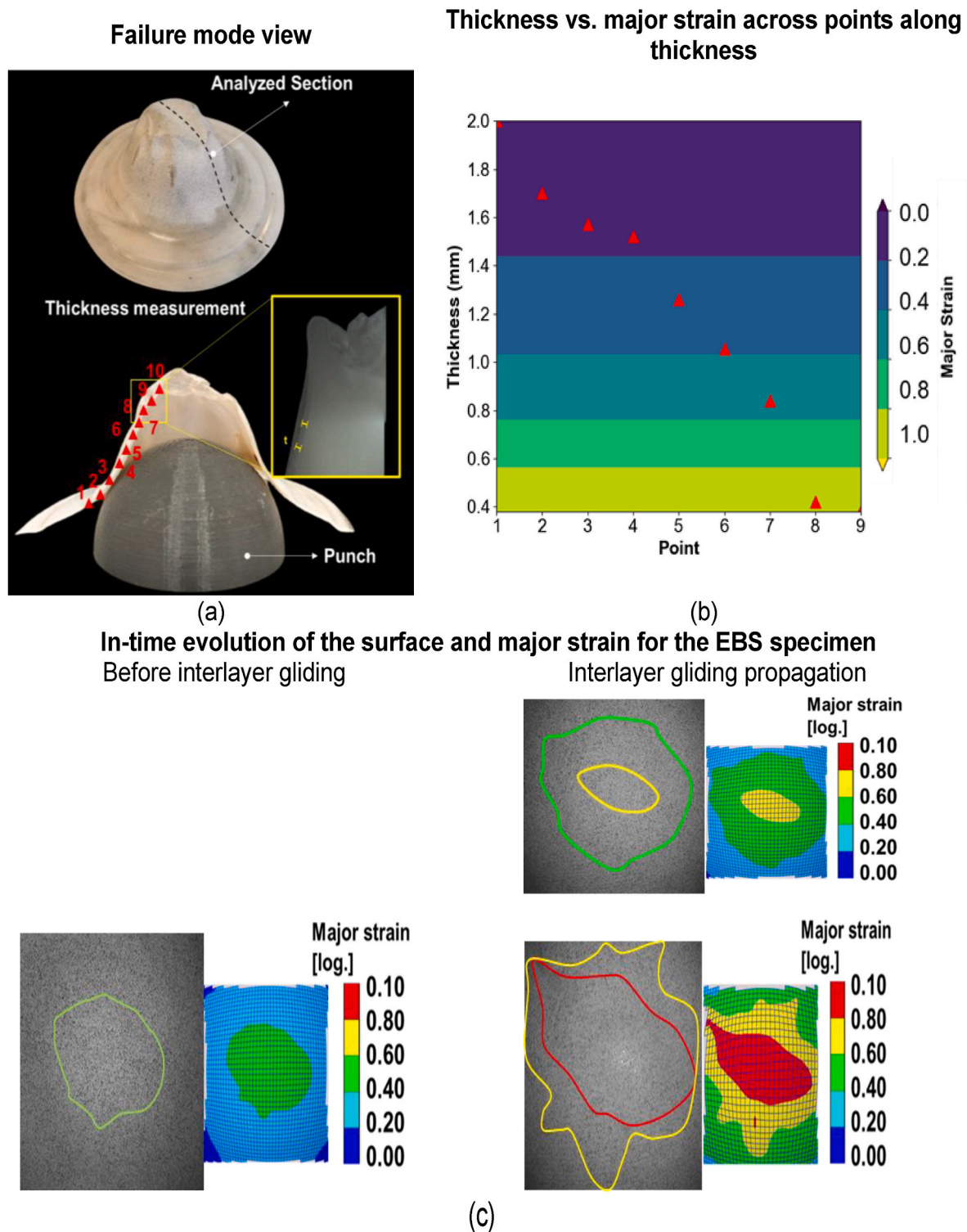Interlayer gliding propagation

(c)

Fig. 14. (a) Perpendicular cross-sectional view of the specimen and thickness measurement. (b) Thickness versus major strain across points along thickness. (c) Evolution of the surface and the major strain over time for the EBS specimen.

material experienced a new failure mode associated with layer sliding capable of propagating until the end of the test (red bars in the interlayer gliding zone). This interlayer gliding failure mode may be a concern to consider when deform FDM-printed sheets, including their characterization.

The melting temperature of PETG ranges between 250 and 260 °C, while that of PCL is around 60 °C. PETG material is printed layer by layer at 250 °C, and the preceding layer onto which the next is extruded is in a much colder state than the layer deposited at that moment. In the case of PCL, which melts at 60 °C, the layers being printed are melted at the time of deposition, allowing for better adhesion between all layers. This difference in cooling ability between PETG and PCL is due to several physical and thermal properties. Among them are thermal conductivity and specific heat capacity. PETG has a thermal conductivity of 0.15–0.3 W/mK, while PCL ranges from 0.1 to 0.2 W/mK [32]. Materials with higher thermal conductivity will dissipate heat more rapidly, thus
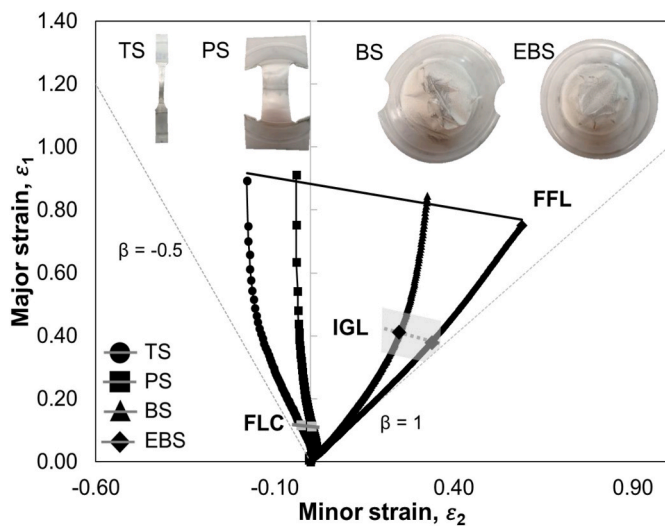
Fig. 15. Formability limits for 3D printed PCL sheets with 2 mm thickness obtained by means of Nakajima specimens.

cooling faster. Regarding the specific heat capacity, PETG ranges from 1.0 to 1.2 J/(g·K), whereas PCL ranges from 1.5 to 1.7 J/(g·K) [32]. In this sense, materials with a higher specific heat capacity can retain more heat before cooling down.

Furthermore, the glass transition temperatures (Tg) of each material are significant factors, with PETG exhibiting a Tg of 80 °C and PCL of −60 °C [32]. In the case of PETG, deformation occurs at room temperature (25 °C), which is below its glass transition temperature. When temperatures fall below Tg, polymeric materials tend to show increased rigidity and brittleness, restricted by limited molecular mobility, resulting in more brittle behavior of the material [33].

In contrast, PCL experiences deformation at room temperature, surpassing its glass transition temperature. Above this critical temperature, the material undergoes a transformation, becoming more pliable, flexible, and less rigid [33]. This shift from a rigid to a more adaptable state is frequently linked to increased molecular mobility, facilitating easier movement of polymer chains. Consequently, the material exhibits a more ductile behavior.

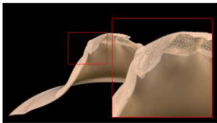However, as indicated in the methodology section, to avoid clogging
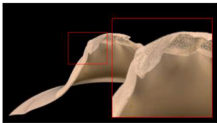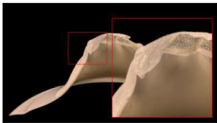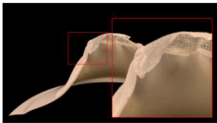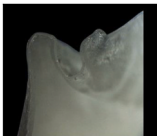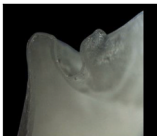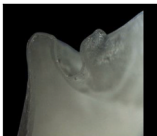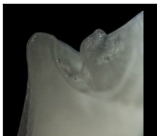
problems, the temperature used to print PCL was a value in the upper range recommended by the manufacturer, specifically at 160 °C. This caused the filament to be printed and deposited on the printing bed so viscous that the deposited filament was not as circular as in the case of PETG, but rather because of the fact that the temperature was flatter, causing a drastic decrease of the intrinsic porosity associated with FDM, resulting in very good adhesion between layers (through thickness and in the same layer). Then, a very homogeneous PCL sheet was obtained, almost without differences between layers, as if it were not printed by FDM.

Undoubtedly, this difference between the bonding layer of the printed sheets for both materials is consistent with the behavior observed and the results obtained during the Nakajima experiment. Precisely due to the characteristics of PCL itself, together with its printing, which allows it to be more homogeneous, it exhibits a behavior different from that of PETG, which provokes this new failure mode of PCL. Clearly, the layer structure of PETG avoids an possibility of the appearance of interlayer gliding.

Finally, this investigation aims to characterize the plastic behavior and failure of FDM-produced polymer materials with the intention of providing an analytical framework for other manufacturing processes. With this analytical framework (based on experimental results), a global context for the comprehensive analysis of such printed materials subjected to further forming processes (such as conventional plastic deformation using press-working machines, punches, and/or dies, as well as other nonproportional and non-conventional forming processes) is provided. In this regard, it will enable the evaluation of hybrid manufacturing processes involving additive manufacturing and incremental forming (single point incremental forming, SPIF), which the authors are currently working on. The PETG material, as evaluated, exhibits low ductility behavior due to the aforementioned characteristics. Therefore, during the SPIF process, the material will be subject to various failure mechanisms, such as cracking, burnout, or porosity, among others [22]. On the other hand, PCL shows good ductile behavior, with its primary failure mode described in this article as interlayer gliding. The authors' objective is to assess the results obtained by SPIF from printed PCL sheets and compare them with those obtained through conventional processes. In this context, the study by Bagudanch et al. [34] assessed the spifability of a PCL sheet material made through compression molding, focusing on the effect of spindle speed on SPIF. Indeed, the PCL exhibited varying failure modes at different speeds, with

Table 6
Summary of the results obtained in terms of principal strain, thickness reduction, and type of failure for PETG and PCL.

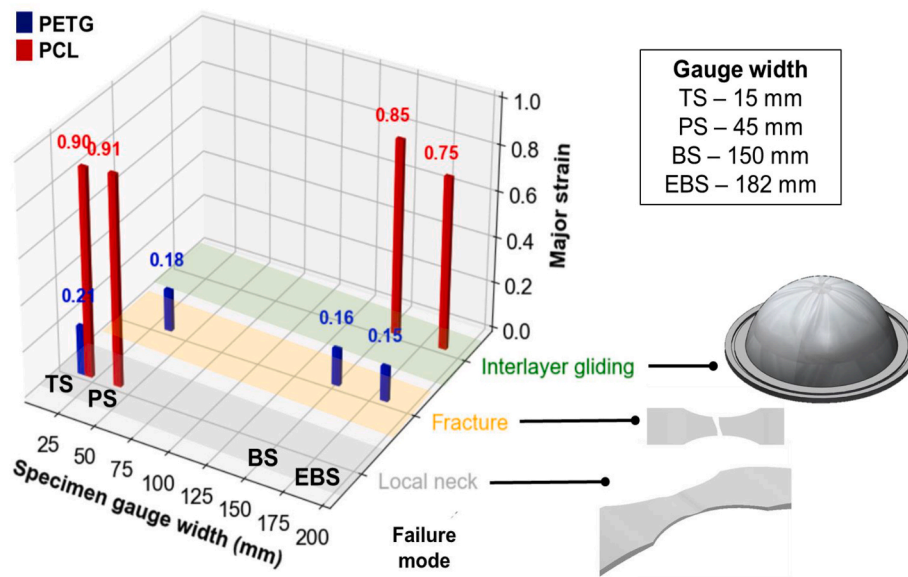| PETG				PCL			
TS	PS	BS	EBS	TS	PS	BS	EBS
Maximum ε_1							
0.21	0.18	0.16	0.15	0.90	0.91	0.85	0.75
Maximum thickness reduction (%)							
13.3	16.0	18.8	17.5	51.1	58.1	69.0	73.8
Failure							
LN	F	F	F	LN	LN	IG	IG
Specimen view							
Enlarged view							

Fig. 16. In 3D, visual representation of the results obtained in terms of the major strain and failure mode based on the gauge width of each specimen.

greater deformation observed at lower speeds, and thus the increase in formability might not be uniquely due to temperature rise with higher speed. Compression-molded PCL achieved a major strain of 0.88, whereas PCL printed using FDM achieved a similar higher strain of 0.91, indicating a slightly better formability due to improved plate homogeneity and prevention of molding defects attained using FDM. Consequently, it is expected that the strains achieved through SPIF will exceed this maximum strain based on earlier research findings [20,35]. This result serves to illustrate the potential of the hybrid additive manufacturing and SPIF process, highlighting its feasibility for various applications.

5. Conclusions

This work presents several contributions in the context of additive manufacturing of materials using FDM. The main contributions are aligned with the comprehensive characterization of the forming limits of two polymeric sheet materials 3D printed using FDM technology, marking a pioneering endeavour in this field. Prior investigations in the literature dealing with formability of FDM printed materials have only made use of conventional tensile or compression tests for evaluating the plastic behavior, offering a limited perspective. Central in the analysis of sheet formability, both in research and industrial contexts, is the Forming Limit Diagram (FLD). This study established methodologies to assess FLDs for FDM printed materials, such as PETG and PCL, and uncovered new configurations of these limits, identifying and analyzing novel types of modes of failure intrinsically linked to the material's structure, stemming from the intricacies of the 3D printing process. On the other hand, this is a necessary first step for a future analysis of other forming processes to which those printed materials could be submitted, providing the resulting FLDs the conventional forming limits and corresponding modes of failure of the materials studied.

To this respect, a comprehensive framework for the study and analysis of hybrid processes has been developed considering the characterization of materials manufactured using additive manufacturing and their subsequent shaping, either through conventional means or through innovative shaping processes such as incremental forming.

Furthermore, specific conclusions can be reached: in the case of PETG material: (i) all the tested specimens displayed low ductile behavior, indicating low formability levels. (ii) Regarding the failure modes, only the specimen subjected to tensile strain showed localized necking, while fracture occurred in plane, biaxial, and equibiaxial strain

specimens. The primary reason behind this was the lack of cohesion between the layers, which promoted this early fracture.

However, from the analysis and evaluation of PCL material printed through additive manufacturing, the following specific conclusions were drawn: (i) the material exhibited high formability levels, to the extent that none of the specimens fractured during the tests. (ii) Regarding failure modes, specimens subjected to tensile and plane strain showed localized necking. However, biaxial and equibiaxial strain specimens displayed a different failure mode, termed "interlayer gliding" in this study. This interlayer gliding was identified as a very weak film of material that did not undergo a proper fracture.

CRediT authorship contribution statement

A. Rosa-Sainz: Writing – original draft, Investigation, Formal analysis, Conceptualization. **I. Ferrer:** Supervision, Methodology, Conceptualization, Writing – review & editing. **M.L. Garcia-Romeu:** Conceptualization, Formal analysis, Funding acquisition, Investigation, Supervision, Writing – review & editing. **G. Centeno:** Conceptualization, Funding acquisition, Methodology, Supervision, Writing – review & editing.

Declaration of competing interest

The authors declare that they have no known competing financial interests or personal relationships that could have appeared to influence the work reported in this paper.

Data availability

Data will be made available on request.

Acknowledgements

References

[1] T.D. Ngo, A. Kashani, G. Imbalzano, K.T.Q. Nguyen, D. Hui, Additive manufacturing (3D printing): a review of materials, methods, applications and challenges, Compos. B Eng. 143 (2018) 172–196, https://doi.org/10.1016/j.compositesb.2018.02.012.

[2] M. Attaran, The rise of 3-D printing: the advantages of additive manufacturing over traditional manufacturing, Bus. Horiz. 60 (2017) 677–688, https://doi.org/10.1016/J.BUSHOR.2017.05.011.

[3] V. Shanmugam, D.J.J. Rajendran, K. Babu, S. Rajendran, A. Veerasimman, U. Marimuthu, S. Singh, O. Das, R.E. Neisiany, M.S. Hedenqvist, F. Berto, S. Ramakrishna, The mechanical testing and performance analysis of polymer-fibre composites prepared through the additive manufacturing, Polym. Test. 93 (2021) 106925, https://doi.org/10.1016/j.polymertesting.2020.106925.

[4] X. Li, A. Heidari, S.M. Nourbakhsh, R. Mohammadi, D. Semiromi, Design and fabrication of elastic two-component polymer-metal disks using a 3D printer under different loads for the lumbar spine, Polym. Test. 112 (2022), https://doi.org/10.1016/j.polymertesting.2022.107633.

[5] J. Kang, Y. Tian, J. Zheng, D. Lu, K. Cai, L. Wang, D. Li, Functional design and biomechanical evaluation of 3D printing PEEK flexible implant for chest wall reconstruction, Comput. Methods Progr. Biomed. 225 (2022), https://doi.org/10.1016/j.cmpb.2022.107105.

[6] E. Polonio-Alcalá, M. Rabionet, A.J. Guerra, M. Yeste, J. Ciurana, T. Puig, Screening of additive manufactured scaffolds designs for triple negative breast cancer 3D cell culture and stem-like expansion, Int. J. Mol. Sci. 19 (2018), https://doi.org/10.3390/ijms19103148.

[7] C.X.F. Lam, X.M. Mo, S.H. Teoh, D.W. Hutmacher, Scaffold development using 3D printing with a starch-based polymer, Mater. Sci. Eng. C 20 (2002) 49–56, https://doi.org/10.1016/S0928-4931(02)00012-7.

[8] F. Ghorbani, A. Zamanian, M. Sahranavard, Modification of freeze-cast poly (E-caprolactone) scaffolds for, Bone Tissue Engineering Applications 65 (2019) 273–287.

[9] A. Rosa-Sainz, M.L. García-Romeu, I. Ferrer, M.B. Silva, G. Centeno, On the effective peek application for customized cranio-maxillofacial prostheses: an experimental formability analysis, J. Manuf. Process. 86 (2023) 66–84, https://doi.org/10.1016/J.JMAPRO.2022.12.044.

[10] W. Lin, H. Shen, G. Xu, L. Zhang, J. Fu, X. Deng, Single-layer temperature-adjusting transition method to improve the bond strength of 3D-printed PCL/PLA parts, Compos Part A Appl Sci Manuf 115 (2018) 22–30, https://doi.org/10.1016/j.compositesa.2018.09.008.

[11] D.M.B. Lopez, R. Ahmad, Tensile mechanical behaviour of multi-polymer sandwich structures via fused deposition modelling, Polymers 12 (2020), https://doi.org/10.3390/polym12030651.

[12] S. Pitjamit, K. Thunsiri, W. Nakkiew, T. Wongwichai, P. Pothacharoen, W. Wattanutchariya, The possibility of interlocking nail fabrication from FFF 3D printing PLA/PCL/HA composites coated by, Materials 13 (2020).

[13] L. Jeantet, A. Regazzi, A. Taguet, M.F. Pucci, A.S. Caro, J.C. Quantin, Biopolymer blends for mechanical property gradient 3d printed parts, Express Polym. Lett. 15 (2021) 137–152, https://doi.org/10.3144/expresspolymlett.2021.13.

[14] R. Kumar, R. Singh, I. Farina, On the 3D printing of recycled ABS, PLA and HIPS thermoplastics for structural applications, PSU Research Review 2 (2018) 115–137, https://doi.org/10.1108/PRR-07-2018-0018.

[15] C. Phillips, M. Kortschot, F. Azhari, Towards standardizing the preparation of test specimens made with material extrusion: review of current techniques for tensile testing, Addit. Manuf. 58 (2022) 103050, https://doi.org/10.1016/j.addma.2022.103050.

[16] X. Gao, S. Qi, X. Kuang, Y. Su, J. Li, D. Wang, Fused filament fabrication of polymer materials: a review of interlayer bond, Addit. Manuf. 37 (2021) 101658, https://doi.org/10.1016/j.addma.2020.101658.

[17] A. Sola, W.J. Chong, D. Pejak Simunec, Y. Li, A. Trinchi, I. Louis Kyratzis, C. Wen, Open challenges in tensile testing of additively manufactured polymers: a literature survey and a case study in fused filament fabrication, Polym. Test. 117 (2023) 107859, https://doi.org/10.1016/j.polymertesting.2022.107859.

[18] L.M. Lozano-Sánchez, I. Bagudanch, A.O. Sustaita, J. Iturbe-Ek, L.E. Elizalde, M.L. Garcia-Romeu, A. Elías-Zúñiga, Single-point incremental forming of two biocompatible polymers: an insight into their thermal and structural properties, Polymers 10 (2018) 391, https://doi.org/10.3390/POLYM10040391, 391 10 (2018).

[19] A. Rosa-Sainz, G. Centeno, M.B. Silva, J.A. López-Fernández, A.J. Martínez-Donaire, C. Vallellano, On the determination of forming limits in polycarbonate sheets, Materials 13 (2020) 1–17, https://doi.org/10.3390/ma13040928.

[20] A. Rosa-Sainz, G. Centeno, M.B. Silva, C. Vallellano, Experimental failure analysis in polycarbonate sheet deformed by spif, J. Manuf. Process. 64 (2021) 1153–1168, https://doi.org/10.1016/j.jmapro.2021.01.047.

[21] A. Rosa-sainz, M.B. Silva, A.M. Beltran, G. Centeno, C. Vallellano, Assessing formability and failure of UHMWPE sheets through SPIF : a case study in medical applications, Polymers 15 (2023) 3560, https://doi.org/10.3390/POLYM15173560.

[22] M.L. Garcia-Romeu, I. Ferrer, C. Pasotti, J. Coma, A. Rosa-Sainz, G. Centeno, Preliminary study on the use of 3D printed biodegradable polymeric sheet for the manufacturing of medical prostheses by SPIF, in: Procedia CIRP, Elsevier B.V., 2022, pp. 76–81, https://doi.org/10.1016/j.procir.2022.06.016.

[23] N. Elmrabet, P. Siegkas, Dimensional considerations on the mechanical properties of 3D printed polymer parts, Polym. Test. 90 (2020), https://doi.org/10.1016/j.polymertesting.2020.106656.

[24] D.M.B. Lopez, R. Ahmad, Tensile mechanical behaviour of multi-polymer sandwich structures via fused deposition modelling, Polymers 12 (2020), https://doi.org/10.3390/polym12030651.

[25] ISO12004-2, Metallic Materials-Sheet and Strip-Determination of Forming Limit Curves Part 2: Determination of Forming Limit Curves in Laboratory, 2008.

[26] A.J. Martínez-Donaire, F.J. García-Lomas, C. Vallellano, New approaches to detect the onset of localised necking in sheets under through-thickness strain gradients, Mater. Des. 57 (2014) 135–145, https://doi.org/10.1016/j.matdes.2014.01.012.

[27] Z. Marciniak, J.L. Duncan, S.J. Hu, Mechanics of Sheet Metal Forming, Butterworth-Heinemann, Oxford, 2002.

[28] A. Rosa-Sainz, G. Centeno, M.B. Silva, J.A. López-Fernández, A.J. Martínez-Donaire, C. Vallellano, On the determination of forming limits in polycarbonate sheets, Materials 13 (2020) 1–17, https://doi.org/10.3390/ma13040928.

[29] A.Y. Al-Maharma, S.P. Patil, B. Markert, Effects of porosity on the mechanical properties of additively manufactured components: a critical review, Mater. Res. Express 7 (2020), https://doi.org/10.1088/2053-1591/abcc5d.

[30] B. Ergene, Ç. Bolat, An experimental investigation on the effect of test speed on the tensile properties of the petg produced by additive manufacturing, International Journal of 3D Printing Technologies and Digital Industry (2022), https://doi.org/10.46519/ij3dptdi.1069544.

[31] J.M. Mercado-Colmenero, M. Dolores La Rubia, E. Mata-Garcia, M. Rodriguez-Santiago, C. Martin-Doñate, Experimental and numerical analysis for the mechanical characterization of petg polymers manufactured with fdm technology under pure uniaxial compression stress states for architectural applications, Polymers 12 (2020) 1–25, https://doi.org/10.3390/polym12102202.

[32] J. Massy, Physical properties of polymers. https://doi.org/10.1007/978-3-319-54831-9_7, 2017.

[33] A. Shrivastava, Introduction to plastics engineering. https://doi.org/10.1016/b978-0-323-39500-7.00001-0, 2018.

[34] I. Bagudanch, G. Centeno, C. Vallellano, M.L. Garcia-Romeu, Revisiting formability and failure of polymeric sheets deformed by Single Point Incremental Forming, Polym. Degrad. Stabil. 144 (2017) 366–377, https://doi.org/10.1016/j.polymdegradstab.2017.08.021.

[35] A. Rosa-Sainz, G. Centeno, M.B. Silva, C. Vallellano, Experimental investigation of polycarbonate sheets deformed by SPIF: formability, micro-mechanisms of failure and temperature analysis, J. Mater. Res. Technol. 25 (2023) 7546–7565, https://doi.org/10.1016/j.jmrt.2023.07.075.